Supplementary Information

Lithium-induced reconstruction of $Li_4Ti_5O_{12}$ for acidic H_2O_2 production via two-electron water oxidation

Yi Wang, Qi Qian, Zehua Zou*, Xuan Zheng, Qinghua Wang, Yun Ling and Qingxiang Wang*

College of Chemistry, Chemical Engineering and Environmental, Fujian Provincial Key Laboratory of Modern Analytical Science and Separation Technology, Minnan Normal University, Zhangzhou 363000, P. R. China

Corresponding email: zzh2221@mnnu.edu.cn; axiang236@vip.163.com

Experimental section

1. Materials

Titanium foil (TF, 99.999%, 0.2 mm thickness) used as the substrate was purchased from Wenghou Metal Material Firm, China. Sodium hydroxide (NaOH, 96.0%), lithium hydroxide (LiOH, 99.8%), sodium sulfate anhydrous (Na_2SO_4, 99.0%), sodium fluoride (NaF, 98.0%), hydrochloric acid (HCl, 35.0%~37.0%), sulfuric acid (H_2SO_4, 95.0%~98.0%) were purchased from Xilong Scientific Co., China. Titanium oxide particles with anatase or rutile structure (TiO_2 anatase or TiO_2 rutile, 99.9%, $\phi = 20$ nm) was purchased from MREDA Technology Inc., USA. All of the chemicals were used as purchased without further purification. Ultrapure water (18 MΩ·cm) was used throughout the experiments.

2. Synthesis of working electrodes

The TF was initially cut into 2 cm × 3 cm rectangles, followed by sequential 1-hour ultrasonic cleanings in ethanol and ultrapure water to remove organic residues and particulate impurities. Then, the cleaned TF was immersed in a 15 mL aqueous solution containing 5 M NaOH with varying NaF additions (0-0.3 g). The mixture was subsequently transferred into a 25 mL Teflon-lined stainless-steel autoclave and subjected to reaction at 180°C for 24 h. Upon cooling the autoclave to ambient temperature, sodium titanium oxide layer was in-situ formed on the TF substrate. The resulting electrode was then thoroughly rinsed with ethanol and ultrapure water, followed by immersion in 0.1 M HCl solution for 2 hours. This acid treatment induced an ion-exchange reaction that transformed sodium titanium oxide into the titanium hydrogen oxide. Following another ethanol/ultrapure water rinse, the resulting electrode was immersed in 15 mL of 0.2 M LiOH solution and subjected to secondary hydrothermal treatment at 150°C for 12 h in a 25 mL Teflon-lined autoclave. Following sequential rinsing with ethanol and ultrapure water and subsequent drying at 60°C for 3 h, the Li^+-intercalated precursor electrode is obtained. Ultimately, the resulting electrode was calcined in air at 450°C for 1 h to obtain the $Li_4Ti_5O_{12}$ spinel on the TF substrate ($Li_4Ti_5O_{12}$/TF) electrode. For comparison, a TiO_2/TF control electrode was fabricated by replicating the $Li_4Ti_5O_{12}$/TF synthesis procedure while deliberately

omitting the secondary hydrothermal lithiation step.

3. Physical measurements

The phase compositions were analyzed via powder X-ray diffraction (XRD, D8 Advance-X, Germany) and Raman spectroscopy (Horiba LabRAM HR Evolution, Japan, 514 nm). The morphology and elemental composition were examined using scanning electron microscopy (SEM, ZEISS Sigma 300, Germany). The crystal structure was probed by transmission electron microscopy (TEM, FEI Talos F200X, USA). X-ray photoelectron spectroscopy (XPS, Thermo Scientific K-Alpha, USA) was employed to investigate valence states of the electrocatalyst. The oxygen vacancies were measured by an electron paramagnetic resonance spectrometer (EPR, Bruker EMXplus, Germany).

4. Electrochemical measurements

All electrochemical performance tests were carried out on Donghua DH7003 electrochemical workstation (China) in a 20 mL electrolyte of 50 mM Na_2SO_4 (acidity was adjusted to pH=3 using H_2SO_4) with N_2 saturation. Carbon rod was used as counter electrode, Hg/Hg_2SO_4 electrode (saturated K_2SO_4) as reference electrode, and TF decorated with electrocatalyst as working electrode. Linear sweep voltammetry (LSV) sweeps between 0.8 V and 3.8 V at a scan rate of 50 mV s^{-1} were applied to active the electrocatalytic property. The stability of electrode was assessed by chronoamperometry at 3.4 V vs. RHE and refreshed the electrolyte every hour. All potentials in the main text were converted to the reversible hydrogen electrode (RHE), and the specific conversion formula is as follows:

$$E(\mathrm{RHE}) = E(\mathrm{Hg/Hg_2SO_4}) + 0.652\ \mathrm{V} + 0.059 \times \mathrm{pH}$$

where $E(Hg/Hg_2SO_4)$ is the measured potential against the Hg/Hg_2SO_4 reference electrode, 0.652 V is its standard potential, and the electrolyte pH was 3.

5. Quantative analysis of H_2O_2 product

The cerium method was used to determine the amount of H_2O_2 generated during electrocatalysis by the following reaction equation:

$$2Ce^{4+} + H_2O_2 \rightarrow 2Ce^{3+} + 2H^+ + O_2$$

The detailed experimental and calculating process are as follows: The 0.1 mM $Ce(SO_4)_2$ solution was prepared with 0.5 M H_2SO_4 solution, and precisely diluted with 0.5 M H_2SO_4 solution to obtain 0.02 mM, 0.04 mM, 0.06 mM, 0.08 mM and 0.10 mM Ce^{4+} standard solutions. They were tested by ultraviolet-visible spectrophotometer (UV-1600PC, Mapada, China) to have maximum absorption peak at 319 nm. The linear relationship between absorbance and their respective concentrations of Ce^{4+} was plotted (Fig. S8). Subsequently, 100 μL of the electrolyte was transferred and allowed to react with 6 mL of the Ce^{4+} standard solution under dark conditions. After a two-hour reaction period, the absorbance of the mixture was measured to determine the concentration of H_2O_2 in the electrolyte, thereby quantifying the amount of H_2O_2 generated. Consequently, the concentration of the produced H_2O_2 and the total amount of passed charges can be calculated to ascertain the Faradaic efficiency.

5. Quantative analysis of O_2 product

The calibration curve for O_2 was established using the external standard method by gas chromatography (GC-4000A EWAI TCD, China). Standard gases with O_2 concentrations of 20%, 40%, 60%, 80%, and 100% were prepared in a bag with a total volume of 10 mL by diluting with high-purity N_2. Each standard gas (1 mL) was injected into the GC system, and the peak area of O_2 was recorded. The linear relationship between the O_2 content and the peak area was plotted (Fig. S12). High-purity nitrogen was purged through the H-type cell for 1 h to remove residual air. After sealing the inlet, electrolysis was performed at 3.4 V for 1 h. Then, 1 mL of the gas from the anode compartment was withdrawn with a gas-tight syringe and injected into the GC. The obtained O_2 peak area was substituted into the linear equation to calculate the total amount of O_2 produced to ascertain the Faradaic efficiency.

6. Theoretical calculation

The first-principles calculations of TiO_2 rutile and TiO_2 anatase were performed using the Quantum Espresso (QE) package. The method of projector augmented wave (PAW) is adapted by using the exchange and correlation function of the Perdew-Burke-Ernzerhof (PBE) with generalized gradient approximation (GGA). The spin-polarized DFT+U method was used to correct the strong correlation electron system ($U_{eff/Ti}$ = 3.5

eV) and the DFT-D3 method was used to correct the weak interaction. The cutoff energy of plane-wave basis was 500 eV and the self-consistent field (SCF) energy and force convergence criteria was 1.0×10^{-6} eV and 0.02 eV/Å, respectively. The *k* point of Gamma-center in Brillouin region was selected as 2×3×1. According to the high-resolution TEM (HRTEM) images, the crystal surface of TiO_2 rutile and TiO_2 anatase was selected as (110) and (101), respectively, which contains (2×1) four layers of Ti-O atoms with a 15 Å thickness of vacuum layer.

Table S1 Summary of TiO_2-based electrocatalysts on H_2O_2 production via $2e^-$-WOR.

Electrocatalyst	FE-PR@potential [a]	Stability	Electrolyte	Ref.
TiO_2/FTO	--38 μM h^{-1} cm^{-2} @3.0 V vs. RHE	-	0.5 M $KHCO_3$	1
TiO_2/FTO	18%-2.6 mM h^{-1} cm^{-2} @3.3 V vs. RHE	-	1 M $NaHCO_3$	2
$Ru_{0.08}Ti_{0.92}O_2$/CF	62.8%-72.6 mM h^{-1} cm^{-2} @3.1 V vs. RHE	10 min	2 M $KHCO_3$	3
TiO_x@MCHS/CF	55.5%-2.4 mM h^{-1} cm^{-2} @2.6 V vs. RHE	4 h	3.5 M K_2CO_3 & 0.5 M $KHCO_3$	4
TiO_{2-x}/FTO	54.5%-153.3 μM h^{-1} cm^{-2} @2.1V vs. RHE	12 h	2 M $KHCO_3$	5
$Ni_{0.13}Ti_{0.87}O_{2-y}$/CF	72%-188.4 mM h^{-1} cm^{-2} @2.7 V vs. RHE	100 h	3.5 M K_2CO_3 & 0.5 M $KHCO_3$	6
TiO_2/FTO	4.5%-37.5 μM h^{-1} cm^{-2} @3.2 V vs. RHE	-	1 M $NaHSO_4$	7
C,N-TiO_2/Ti	8%-0.29 μM h^{-1} cm^{-2} @3.3 V vs. RHE	6 h	0.05 M Na_2SO_4 & H_2SO_4 (pH=3)	8
$Li_4Ti_5O_{12}$/TF	3.41%-74.69 μM h^{-1} cm^{-2} @3.4V vs. RHE	120 h	0.05 M Na_2SO_4 & H_2SO_4 (pH=3)	This work

[a]: For consistent comparison across different studies, the values of Faradaic efficiency (FE), H_2O_2 production rate (PR) and potential in Table S1 were calculated or estimated based on raw data and figures from the corresponding references. These calculations were performed to normalize units (e.g., converting to μM h^{-1} cm^{-2} or mM h^{-1} cm^{-2}). Original data sources are provided in the "Ref." column for verification.

References

1 K. Fuku, Y. Miyase, Y. Miseki, T. Gunji and K. Sayama, *ChemistrySelect*, 2016, **1**, 5721-5726.

2 X. Shi, S. Siahrostami, G. L. Li, Y. Zhang, P. Chakthranont, F. Studt, T. F. Jaramillo, X. Zheng and J. K. Norskov, *Nat. Commun.*, 2017, **8**, 701.

3 Z. Wang, W. Xu, G. Tan, X. Duan, B. Yuan, M. G. Sendeku, H. Liu, T. Li, F. Wang, Y. Kuang and X. Sun, *Sci. Bull.*, 2023, **68**, 613–621.

4 Z. Wang, K. Li, J. Hu, A. Li, Y. Tang, Y. Sun, P. Wan, H. Jiang and Y. Chen, *Adv. Funct. Mater.*, 2025, **35**, 2425301.

5 K. Dong, J. Liang, Y. Wang, Y. Ren, Z. Xu, H. Zhou, L. Li, Q. Liu, Y. Luo, T. Li, A. M. Asiri, Q. Li, D. Ma and X. Sun, *Chem. Catal.*, 2021, **1**, 1-12.

6 Z. Wang, X. Duan, M. G. Sendeku, W. Xu, S. Y. Chen, B. Tian, W. Gao, F. Wang, Y. Kuang and X. Sun, *Chem. Catal.*, 2023, **3**, 100672.

7 Z. Chen, S. Geng, J. Xiao, F. Zhao, K. Wang, Y. Wang, P. Tsiakaras and S. Song, *Chem. Eng. J.*, 2022, **431**, 134332.

8 S. Xue, L. Tang, Y. Tang, C. Li, M. Li, J. Zhou, W. Chen, F. Zhu and J. Jiang, ACS Appl. Mater. Interfaces, 2020. 12, 4423-4431.

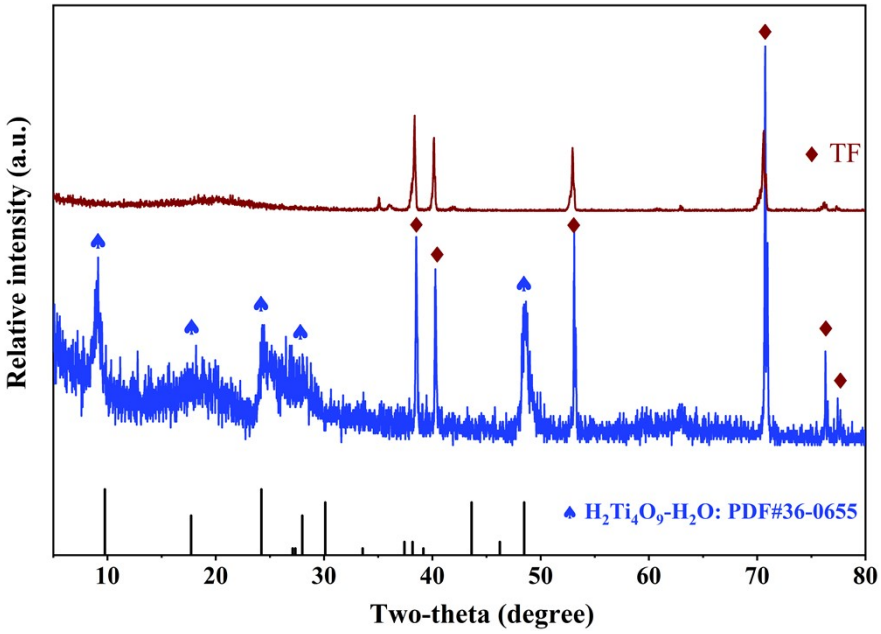

Fig. S1 XRD patterns of $H_2Ti_4O_9$/TF and TF.

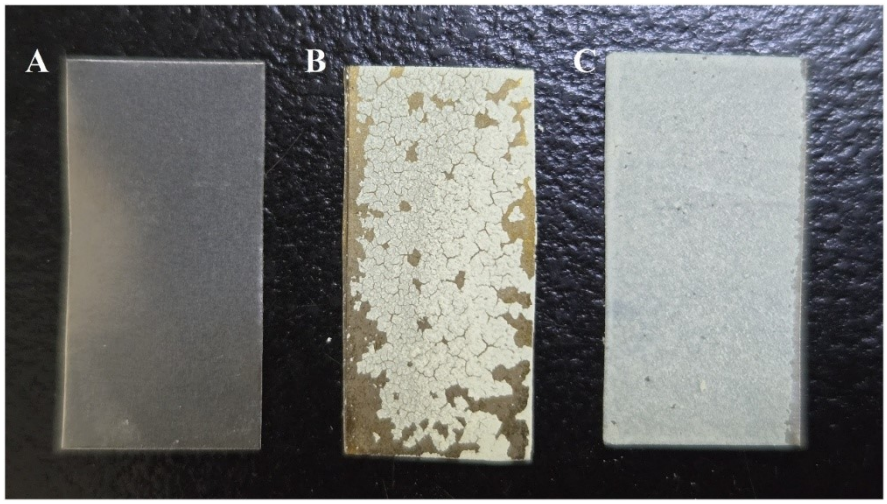

Fig. S2 Photographs of (A) TF, (B) TiO_2/TF and (C) $Li_4Ti_5O_{12}$/TF.

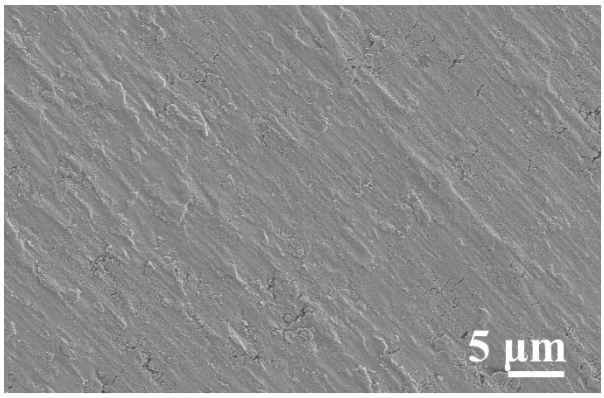

Fig. S3 SEM image of bare Ti foil.

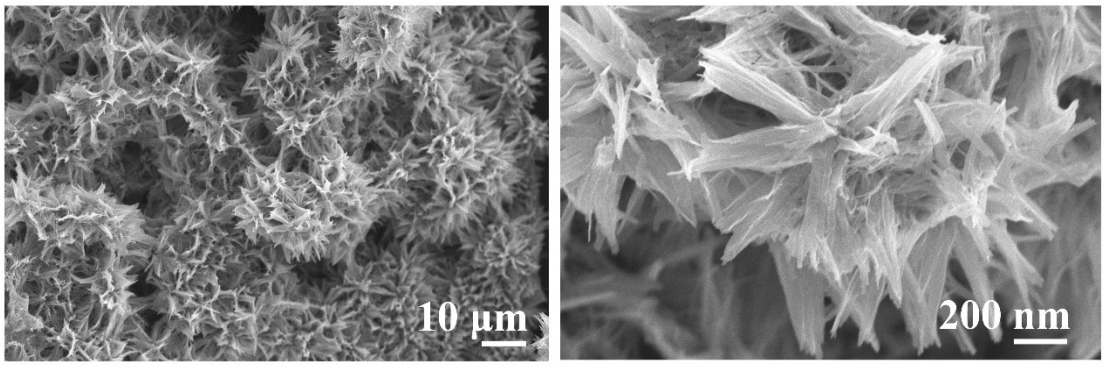

Fig. S4 SEM images of TiO_2 from TiO_2/TF.

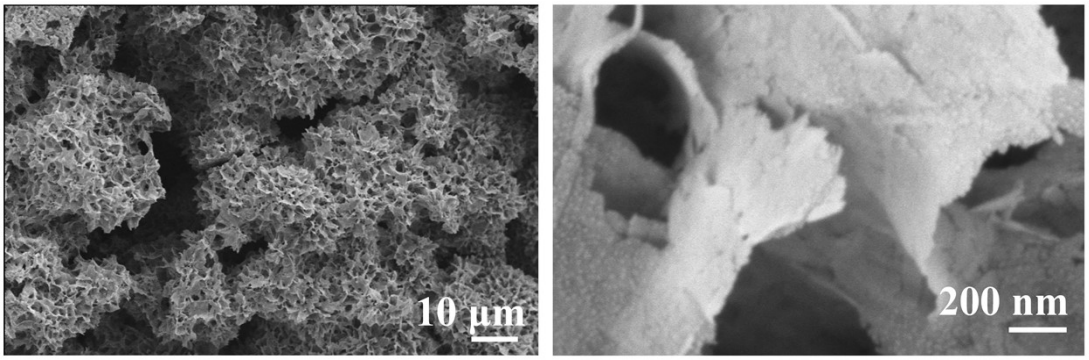

Fig. S5 SEM images of $Li_4Ti_5O_{12}$.

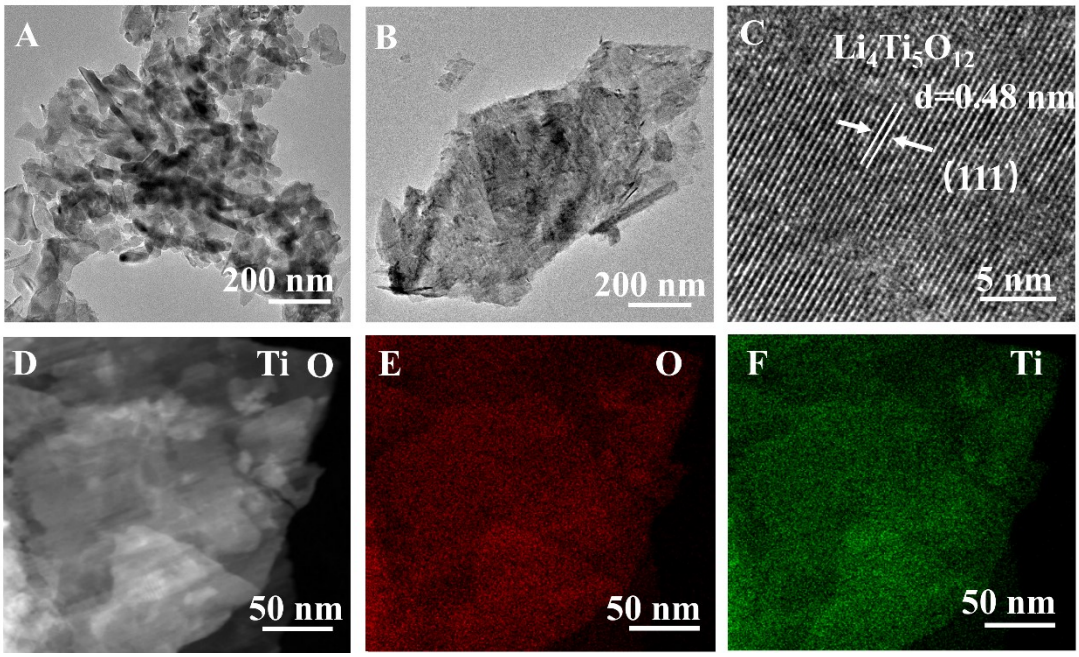

Fig. S6 TEM images of (A) TiO_2 and (B) $Li_4Ti_5O_{12}$. (C) HRTEM image, (D) HAADF-STEM image and (E, F) the elemental mapping images of $Li_4Ti_5O_{12}$.

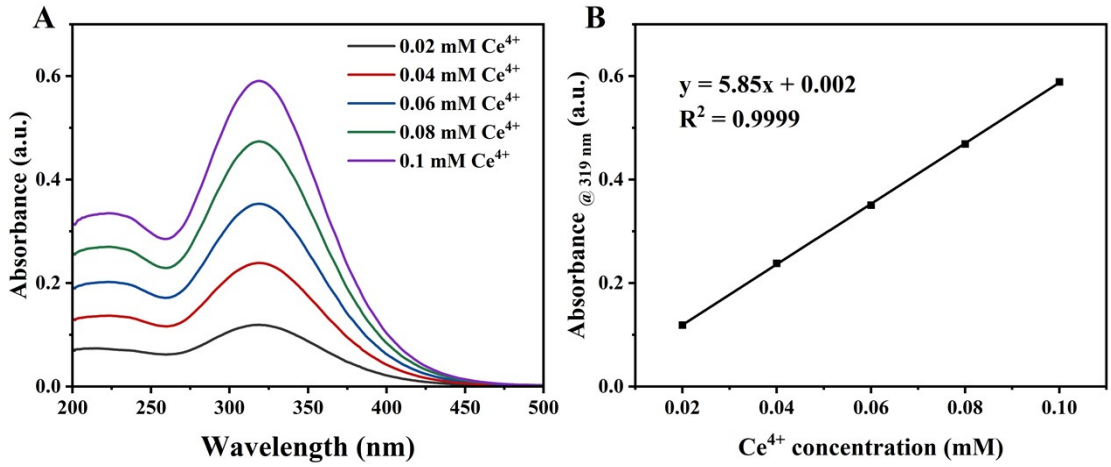

Fig. S7 (A) The UV-vis absorption spectrum of Ce^{4+} solution at different concentrations, and (B) the corresponding calibration curve.

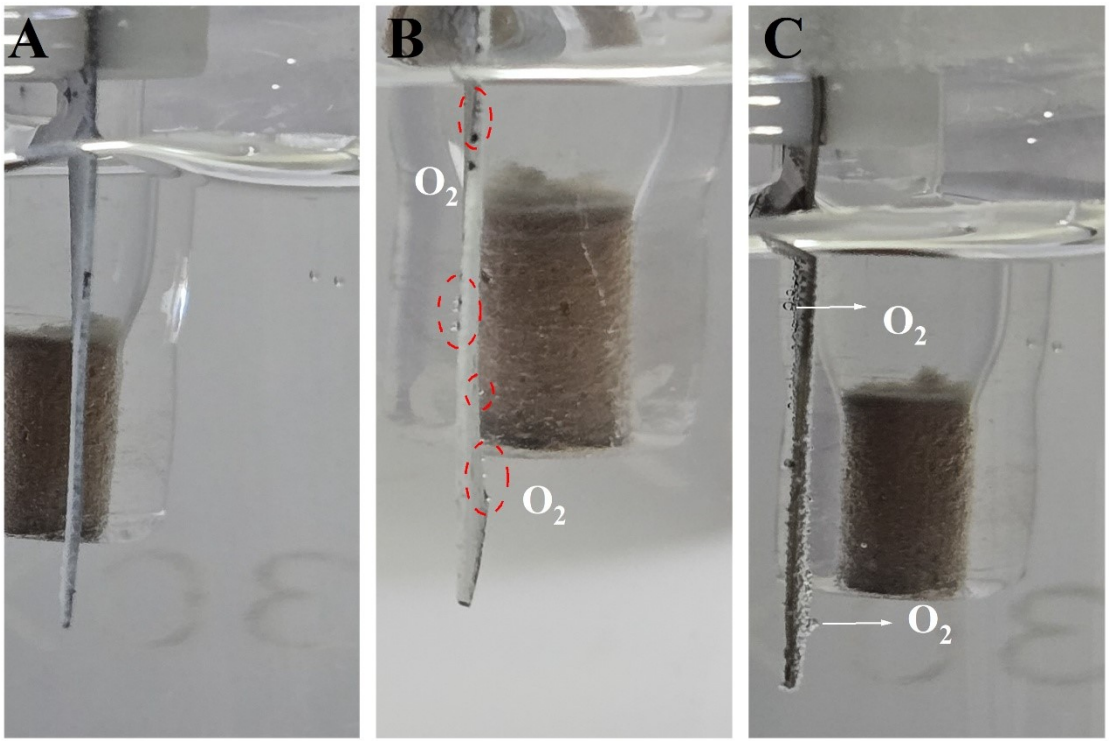

Fig. S8 Photographs of oxygen bubbles on (A) $Li_4Ti_5O_{12}$/TF, (B) TiO_2/TF and (C)TF.

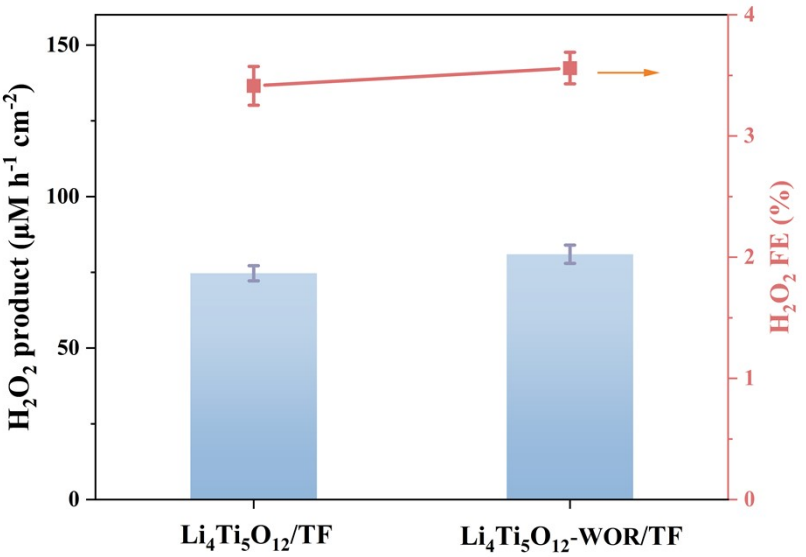

Fig. S9 The performance comparison of $Li_4Ti_5O_{12}$/TF and $Li_4Ti_5O_{12}$-WOR/TF.

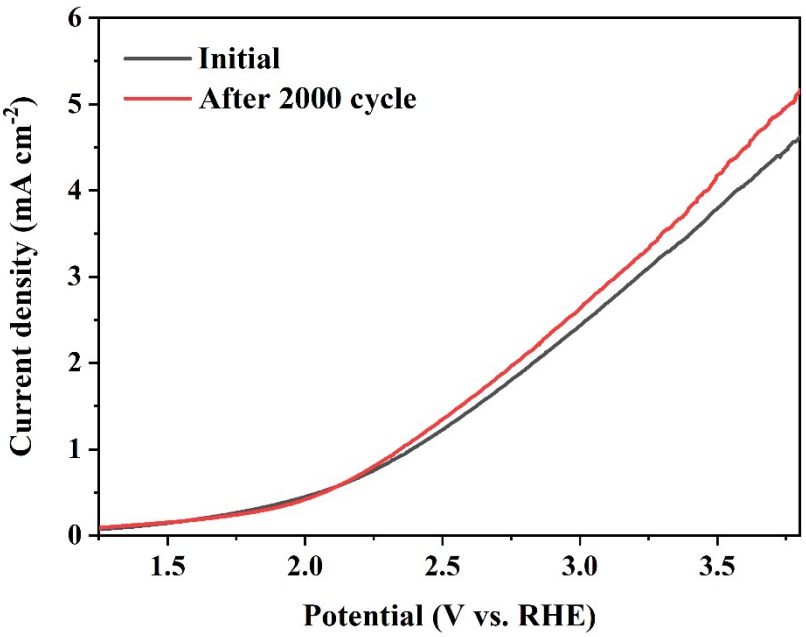

Fig. S10 LSV curves of $Li_4Ti_5O_{12}$/TF before and after 2000 cycles in the stability test.

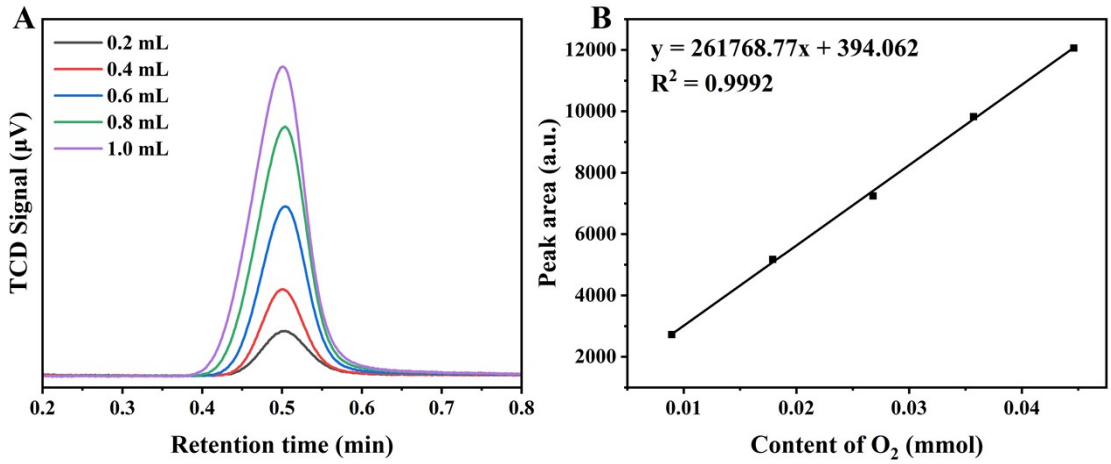

Fig. S11 (A) The gas chromatography curves of O_2 at different volumes, and (B) the corresponding calibration curve.

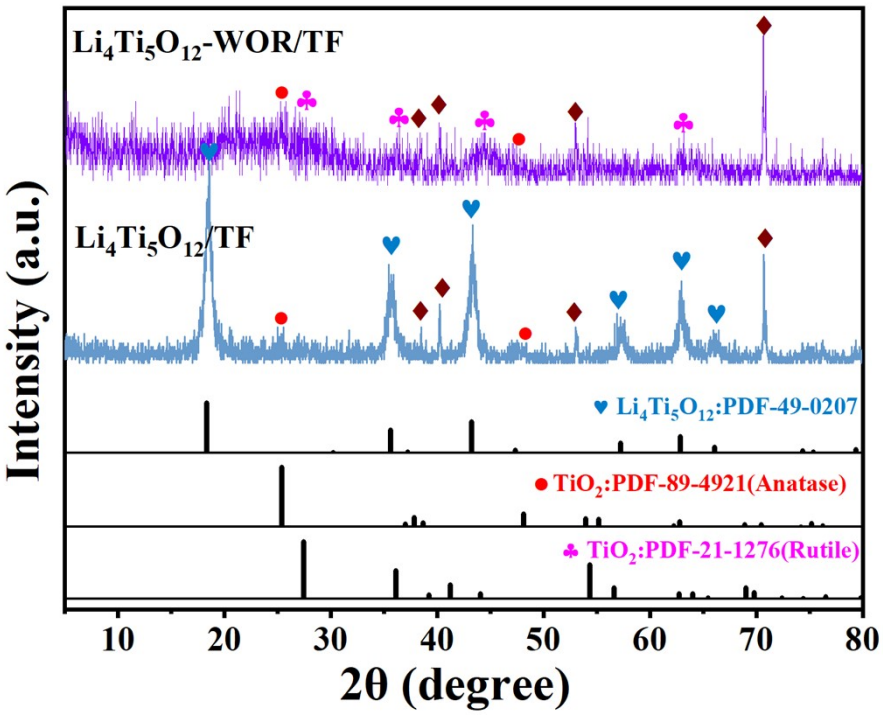

Fig. S12 XRD patterns of $Li_4Ti_5O_{12}$/TF and $Li_4Ti_5O_{12}$-WOR/TF.

Table S2. The element content of $Li_4Ti_5O_{12}$ and $Li_4Ti_5O_{12}$-WOR based on the XPS data. (unit: at %)

	Li	Ti	O
$Li_4Ti_5O_{12}$	16.1	24.7	59.2
$Li_4Ti_5O_{12}$-WOR	0.7	28.6	70.7

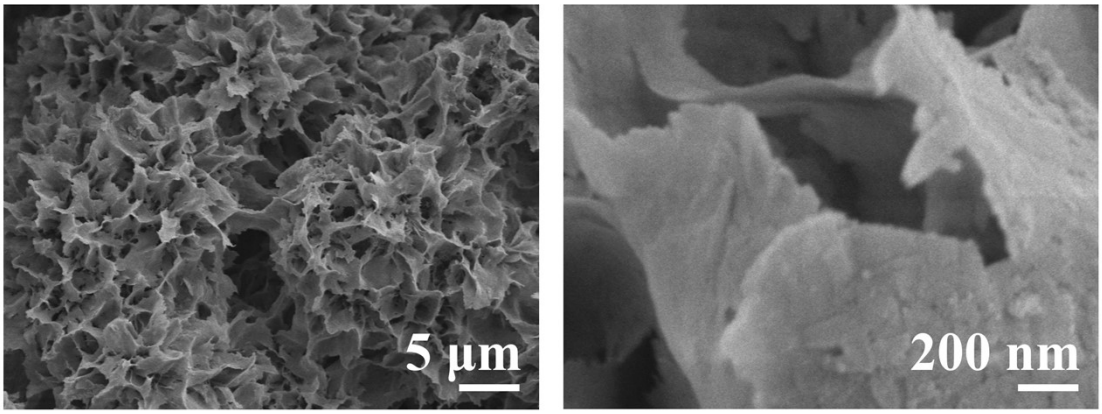

Fig. S13 SEM images of $Li_4Ti_5O_{12}$-WOR.